Global Measurements of Stratospheric Mountain Waves from Space

Stephen D. Eckermann[1] and Peter Preusse[2]

Temperatures acquired by the Cryogenic Infrared Spectrometers and Telescopes for the Atmosphere (CRISTA) during shuttle mission STS-66 have provided measurements of stratospheric mountain waves from space. Large-amplitude, long-wavelength mountain waves at heights of 15 to 30 kilometers above the southern Andes Mountains were observed and characterized, with vigorous wave breaking inferred above 30 kilometers. Mountain waves also occurred throughout the stratosphere (15 to 45 kilometers) over a broad mountainous region of central Eurasia. The global distribution of mountain wave activity accords well with predictions from a mountain wave model. The findings demonstrate that satellites can provide the global data needed to improve mountain wave parameterizations and hence global climate and forecast models.

Gravity waves in the lower atmosphere, forced by flow over mountains, have been observed and modeled for many years (1). Mountain waves can also propagate into the stratosphere. Drag produced by breaking stratospheric mountain waves is essential for accurate climate and forecast models (2). The turbulence generated by stratospheric mountain wave breaking poses a major safety hazard to high-altitude aircraft (3–5) and influences stratosphere-troposphere exchange of important trace gases (6). Mountain wave ascent triggers formation of polar stratospheric clouds (PSCs) (7). It has been argued that mountain wave PSCs reduce Arctic ozone concentrations by activating chlorine in stratospheric air that flows through them (8).

Computational limits have prevented global troposphere-stratosphere models from operating at a spatial resolution fine enough to generate mountain waves in the stratosphere, so their effects must be parameterized (2). The spatial resolution of stratospheric sounding satellites has generally been too coarse to resolve mountain waves. Detailed measurements have been limited largely to scattered ground-based soundings (9), some regional campaigns (3, 10), and chance intercepts by high-altitude aircraft (4, 11). Thus, global data are lacking.

Recently, a few high-resolution stratospheric satellite instruments have detected gravity waves (12). However, instrumental effects have complicated interpretation of these gravity-wave signals (13). In particular,

the data have shown little clear evidence of mountain waves, despite suggestions that mountains should be a strong source of stratospheric gravity waves (2–4, 9–11).

On 4 November 1994, the CRISTA-SPAS (Shuttle Pallet Satellite) experiment was deployed into orbit by the space shuttle Atlantis (Fig. 1A). CRISTA measured infrared emission spectra (4 to 71 μm) from atmospheric limb scans with the use of three telescopes that viewed closely separated volumes of air (14). From the CO_2 Q-branch emission at ~12.6 μm, vertical temperature profiles $T(z)$ with a precision of ~0.5 K were derived every 1.5 km in altitude, z, throughout the stratosphere (15, 16). Although short spatial scales along the line of sight are smeared out, medium scale structure is resolved. Theoretical radiance calculations show that the temperature data have >50% visibility to gravity waves with wavelengths $\gtrsim$3 to 5 km vertically and $\gtrsim$100 to 200 km along the limb (17). Each telescope provided a profile every 200 or 400 km along the orbital track, depending on the measurement mode (18), for a week.

Small-scale temperature fluctuations $T'(z)$ were isolated from global temperature data with a wavenumber 0 to 6 Kalman filter. Vertical wavelengths λ_z and amplitudes $\hat{T}$ of dominant oscillations in each $T'(z)$ profile were determined with spectral peak detection and sliding harmonic fits, respectively. These parameters are shown (Fig. 1B) for three successive $T'(z)$ profiles (labeled 1, 2, and 3) acquired over the southern Andes Mountains (Fig. 1C) on 6 November 1994. All three profiles show similar-looking large-amplitude wave oscillations at 15 to 30 km. The photo in Fig. 1A, taken over this region 2 days earlier, shows banded mountain wave clouds downstream of the Andes. This suggests that the oscillations in Fig. 1B may be stratospheric mountain waves.

A long, stationary plane mountain wave emanating from the Andes should have a vertical wavelength given by the hydrostatic relation

$$(\lambda_z)_{\text{theory}} \approx \frac{2\pi \bar{U}}{N} \qquad (1)$$

where $\bar{U}$ is the local horizontal wind speed across the Andean Ridge and N is the buoyancy frequency (1). At 15 to 30 km, $\bar{U} \approx 20$ to 23 m s^{-1} (Fig. 1D) and $N \approx 0.020$ rad s^{-1}, which yields $(\lambda_z)_{\text{theory}} \approx 6$ to 7 km. The observed vertical wavelength λ_z of the measured wave oscillations in Fig. 1B is ~6.5 km at 15 to 30 km. The close agreement between observed and theoretical vertical wavelengths is strong evidence that these measured wave oscillations are stratospheric mountain waves. Successive profiles are separated horizontally by 200 km (Fig. 1C) and phase shifted by 180° (Fig. 1B). This implies a horizontal wavelength $\lambda_h = 400/n$ km for this wave, where n is an odd integer. Given the sensitivity of CRISTA to $\lambda_h > 100$ to 200 km, then λ_h must be either 130 or 400 km.

Nonbreaking mountain waves grow in amplitude with height approximately as exp($z/2H_\rho$). The density scale height $H_\rho \sim 7$ km, and so $\hat{T}$ should increase by a factor of 3 over the 15- to 30-km height range, as observed in Fig. 1B. Thus, the mountain wave propagates without breaking from 15 to 30 km. Above 30 km, the oscillations in Fig. 1B abruptly attenuate and disappear. There are two plausible reasons for this. Because winds weaken rapidly above this level (Fig. 1D), λ_z decreases according to Eq. 1, and the wave soon becomes too short for CRISTA to resolve. Additionally, however, the wave is likely to break above 30 km. Mountain waves advect heavy air over lighter air and overturn when amplitudes exceed the breaking threshold

$$\hat{T} \geq \hat{T}_{\text{break}} \approx \left[\frac{d\bar{T}}{dz} + \Gamma_a \right] \frac{\bar{U}}{N} \qquad (2)$$

where Γ_a is the adiabatic lapse rate (9.8 K km^{-1}) and $\bar{T}$ is background temperature (19). At 15 to 30 km, the mountain wave-breaking amplitude $\hat{T}_{\text{break}} \approx 10$ K. This value is consistent with the observed nondissipative growth in $\hat{T}$ from 15 to 30 km, because $\hat{T} < \hat{T}_{\text{break}}$ at these heights. At 30 km, however, $\hat{T} = 7$ K (Fig. 1B) and is probably larger in reality, given some observational smearing. Indeed, retrieval calculations indicate that, for a wave of $\lambda_z = 6.5$ km and $\lambda_h = 400$ km, the amplitude $\hat{T}$ measured by CRISTA is only ~60% of its true value (17). Thus, this wave is at or near its breaking amplitude at 30 km. Above 30 km, Eq. 2 shows that $\hat{T}_{\text{break}}$ decreases because of the weakening winds in Fig. 1D, making wave breaking and amplitude attenuation even more probable and severe.

The influence of a breaking mountain wave on the atmosphere is determined by its vertical flux of horizontal momentum density, the so-

[1]E. O. Hulburt Center for Space Research, Naval Research Laboratory, Code 7641.2, Washington, DC 20375, USA. [2]Department of Physics, University of Wuppertal, Gauss-Strasse 20, D-42097 Wuppertal, Germany.

*To whom correspondence should be addressed. E-mail: eckerman@map.nrl.navy.mil

Report Documentation Page

Form Approved
OMB No. 0704-0188

Public reporting burden for the collection of information is estimated to average 1 hour per response, including the time for reviewing instructions, searching existing data sources, gathering and maintaining the data needed, and completing and reviewing the collection of information. Send comments regarding this burden estimate or any other aspect of this collection of information, including suggestions for reducing this burden, to Washington Headquarters Services, Directorate for Information Operations and Reports, 1215 Jefferson Davis Highway, Suite 1204, Arlington VA 22202-4302. Respondents should be aware that notwithstanding any other provision of law, no person shall be subject to a penalty for failing to comply with a collection of information if it does not display a currently valid OMB control number.

1. REPORT DATE **NOV 1999**	2. REPORT TYPE	3. DATES COVERED **00-00-1999 to 00-00-1999**

4. TITLE AND SUBTITLE **Global Measurements of Stratospheric Mountain Waves from Space**	5a. CONTRACT NUMBER
	5b. GRANT NUMBER
	5c. PROGRAM ELEMENT NUMBER
6. AUTHOR(S)	5d. PROJECT NUMBER
	5e. TASK NUMBER
	5f. WORK UNIT NUMBER

7. PERFORMING ORGANIZATION NAME(S) AND ADDRESS(ES) **Naval Research Laboratory,E.O. Hulburt Center for Space Research,Washington,DC,20375**	8. PERFORMING ORGANIZATION REPORT NUMBER

9. SPONSORING/MONITORING AGENCY NAME(S) AND ADDRESS(ES)	10. SPONSOR/MONITOR'S ACRONYM(S)
	11. SPONSOR/MONITOR'S REPORT NUMBER(S)

12. DISTRIBUTION/AVAILABILITY STATEMENT
Approved for public release; distribution unlimited

13. SUPPLEMENTARY NOTES

14. ABSTRACT

15. SUBJECT TERMS

16. SECURITY CLASSIFICATION OF:			17. LIMITATION OF ABSTRACT	18. NUMBER OF PAGES	19a. NAME OF RESPONSIBLE PERSON
a. REPORT **unclassified**	b. ABSTRACT **unclassified**	c. THIS PAGE **unclassified**	**Same as Report (SAR)**	**4**	

Standard Form 298 (Rev. 8-98)
Prescribed by ANSI Std Z39-18

called Eliassen-Palm (EP) flux, which can be computed from measured wave parameters (20). With the use of Eq. 2 and linear saturation theory (2, 19), wave breaking above 30 km yields large EP flux divergences that imply mean-flow accelerations of up to $-(50$ to $200)$ m s^{-1} day^{-1}. These decelerative forces on the eastward stratospheric flow in Fig. 1D are one to two orders of magnitude larger than zonal-mean climatological estimates of small-scale wave forcing at 40° to 50°S (21). Such large values imply vigorous local wave breaking, drag, turbulence production, and mixing at 30 to 40 km. The wave is likely to dissipate entirely below 43 km, where a critical level ($\bar{U} = 0$: Fig. 1D) causes both λ_z and $\hat{T}$ to vanish (Eqs. 1 and 2) and prevents further penetration of mountain wave energy (1).

How common are large mountain wave events? Figure 2 compares λ_z and $(\lambda_z)_{theory}$ at $z = 25$ km based on $T'(z)$ data for all seven mission days at 40° to 50°S over South America. Again, there is very good correlation between theoretical and measured vertical wavelengths. Amplitudes measured on four successive days are plotted in Fig. 3, A to D. Underlying plots show corresponding predictions, with the Naval Research Laboratory Mountain Wave Forecast Model (MWFM) (4, 22) interfaced to assimilated regional winds and temperatures from NASA's Data Assimilation Office (DAO) (Fig. 3, E to G) (23). The MWFM results capture much of the day-to-day variability. Figures 2 and 3 reveal that mountain waves were present in this region of the stratosphere throughout the mission.

These long plane stratospheric mountain waves resemble those observed by aircraft over the Scandinavian Ridge (8, 24). Rapid cooling of air by the latter waves produces PSCs, which in turn destroy Arctic ozone (8). Although the Andean mountain waves observed here also produce large temperature decreases (Fig. 3), they are probably too far north to yield temperatures cold enough to form PSCs. Nevertheless, as the edge of the Antarctic vortex moves back and forth across the tip of South America (25), strong turbulence generated by these mountain waves will mix tongues of ozone-depleted vortex air with ozone-rich air from mid-latitudes, thus diluting local ozone concentrations overall. The large EP flux divergences could also modify the subsequent evolution of the vortex (26).

Are stratospheric mountain waves evident elsewhere in the CRISTA data? $\hat{T}$ amplitudes over the Northern Hemisphere at 25, 35, and 45 km on 9 November 1994 are plotted in Fig. 4, A to C. Mountain wave amplitudes $\hat{T}$ predicted by MWFM on this day are shown in Fig. 4, D and F. Although the peak amplitudes differ (27), observations and model results show very similar geographical distributions. Most notable is a broad region of enhanced amplitudes over central Eurasia. The activity is produced by mountain waves from the Altai Mountains,
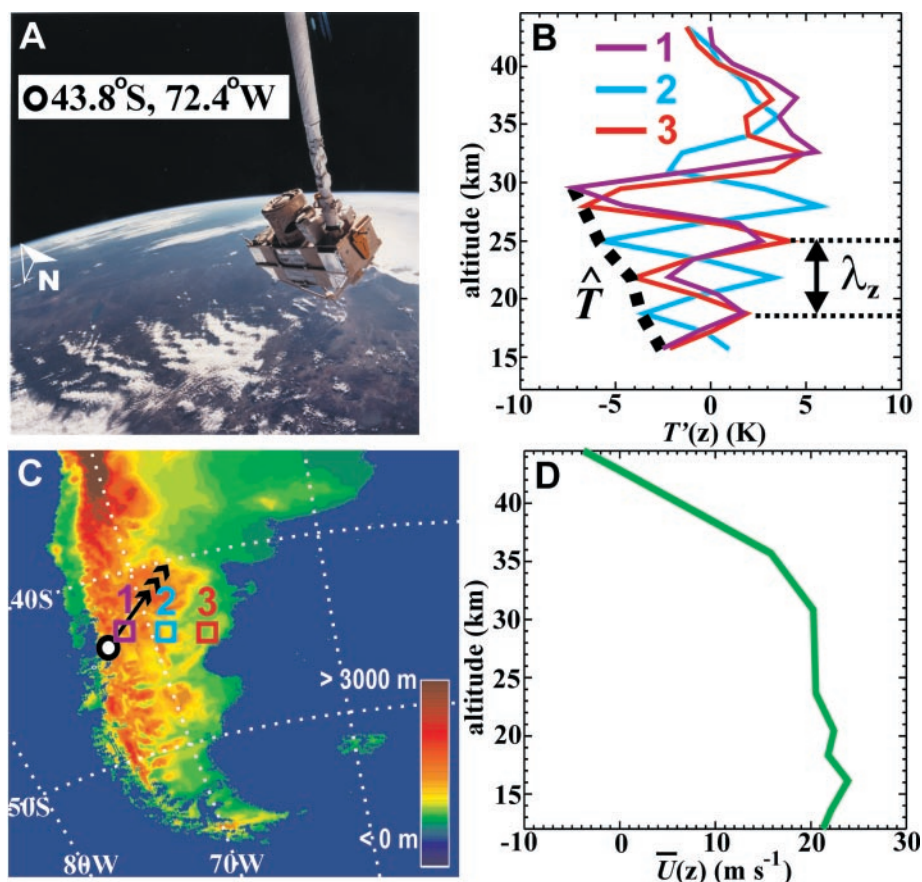

Fig. 1. (**A**) Astronaut photograph over southern South America showing deployment of CRISTA-SPAS from Atlantis, 4 November 1994, at 12:19 UT. The cylindrical assembly on the satellite houses CRISTA. The east coast of Argentina and the Atlantic Ocean are visible to the right; banded mountain wave clouds downstream of the Andes are visible to the lower left. (**B**) Temperature perturbations $T'(z)$ from three successive CRISTA scans (labeled 1, 2, and 3) on 6 November 1994, at ~06:00 UT. (**C**) Topographic elevations for southern South America (linear color scale). Squares labeled 1, 2, and 3 show locations of the profiles in (B). The nadir point and orbital motion of the shuttle in (A) are shown with a black and white circle and black arrow, respectively. (**D**) Horizontal winds orthogonal to the Andean Ridge, from DAO assimilated data (23) at 42°S, 69°W on 6 November 1994, 06:00 UT.
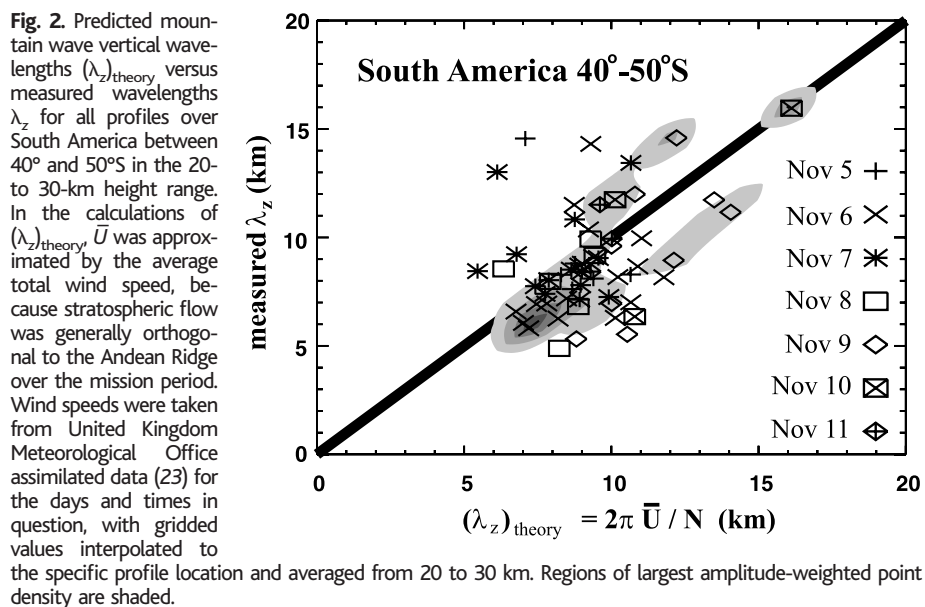
Fig. 2. Predicted mountain wave vertical wavelengths $(\lambda_z)_{theory}$ versus measured wavelengths λ_z for all profiles over South America between 40° and 50°S in the 20- to 30-km height range. In the calculations of $(\lambda_z)_{theory}$, $\bar{U}$ was approximated by the average total wind speed, because stratospheric flow was generally orthogonal to the Andean Ridge over the mission period. Wind speeds were taken from United Kingdom Meteorological Office assimilated data (23) for the days and times in question, with gridded values interpolated to the specific profile location and averaged from 20 to 30 km. Regions of largest amplitude-weighted point density are shaded.

Fig. 3. $\hat{T}$ amplitudes over southern South America from 6 to 9 November 1994 (**A** to **D**, respectively), plotted as color pixels at the profile location. Raw values were scaled according to their vertical wavelengths to correct for observational smearing (*17*). Beneath each panel is a corresponding MWFM prediction based on DAO assimilated winds and temperatures at 12:00 UT for these dates (**E** to **H**). Modeled waves with $\lambda_z < 5$ km were not plotted because CRISTA is not sensitive to them. The color scales are linear. Pixels are plotted in order of ascending amplitude and are sized to maximize coverage and visibility while minimizing pixel overlap.
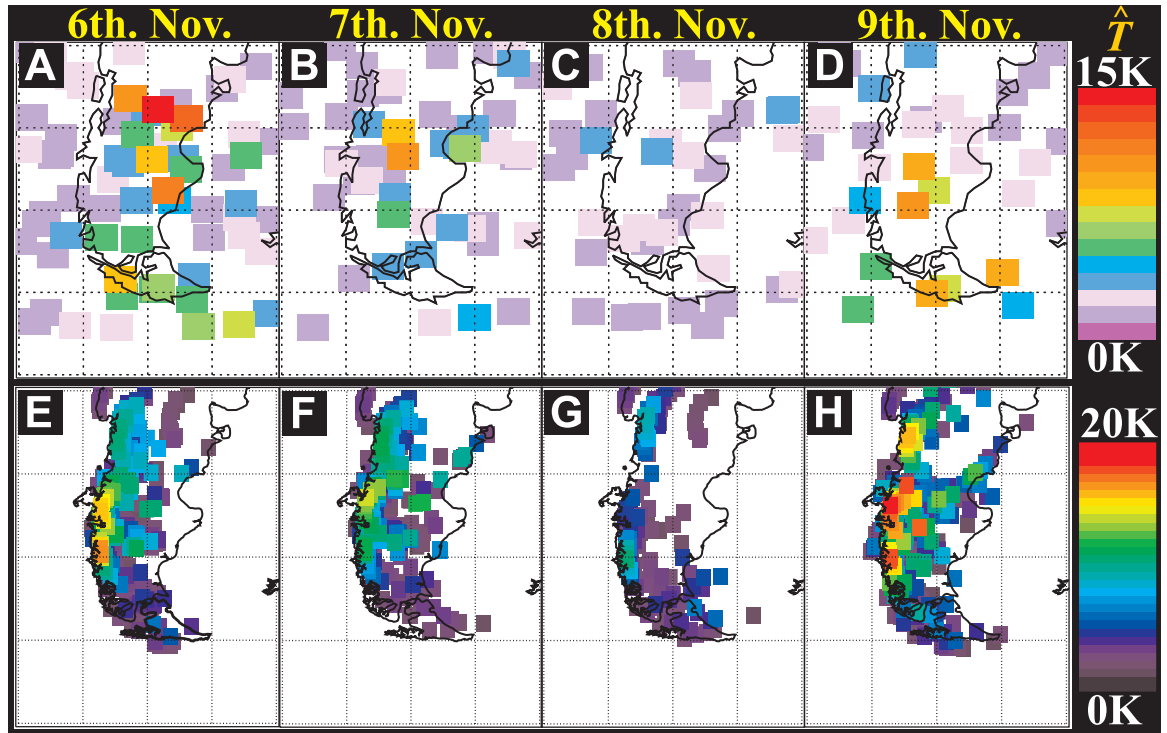

Fig. 4. (**A** to **C**) Polar orthographic maps of amplitudes $\hat{T}$ from CRISTA profiles over the Northern Hemisphere on 9 November 1994 at 25, 35, and 45 km, respectively. Values were corrected for observational smearing as in Fig. 3. (**D** and **F**) Corresponding MWFM amplitudes $\hat{T}$ at 25 and 45 km, respectively, based on DAO assimilated winds and temperatures at 12:00 UT on this date. As in Fig. 3, modeled waves with $\lambda_z < 5$ km were omitted. (**E**) Topographic elevation in the Northern Hemisphere. All color scales are linear. Pixels are plotted in order of ascending amplitude.
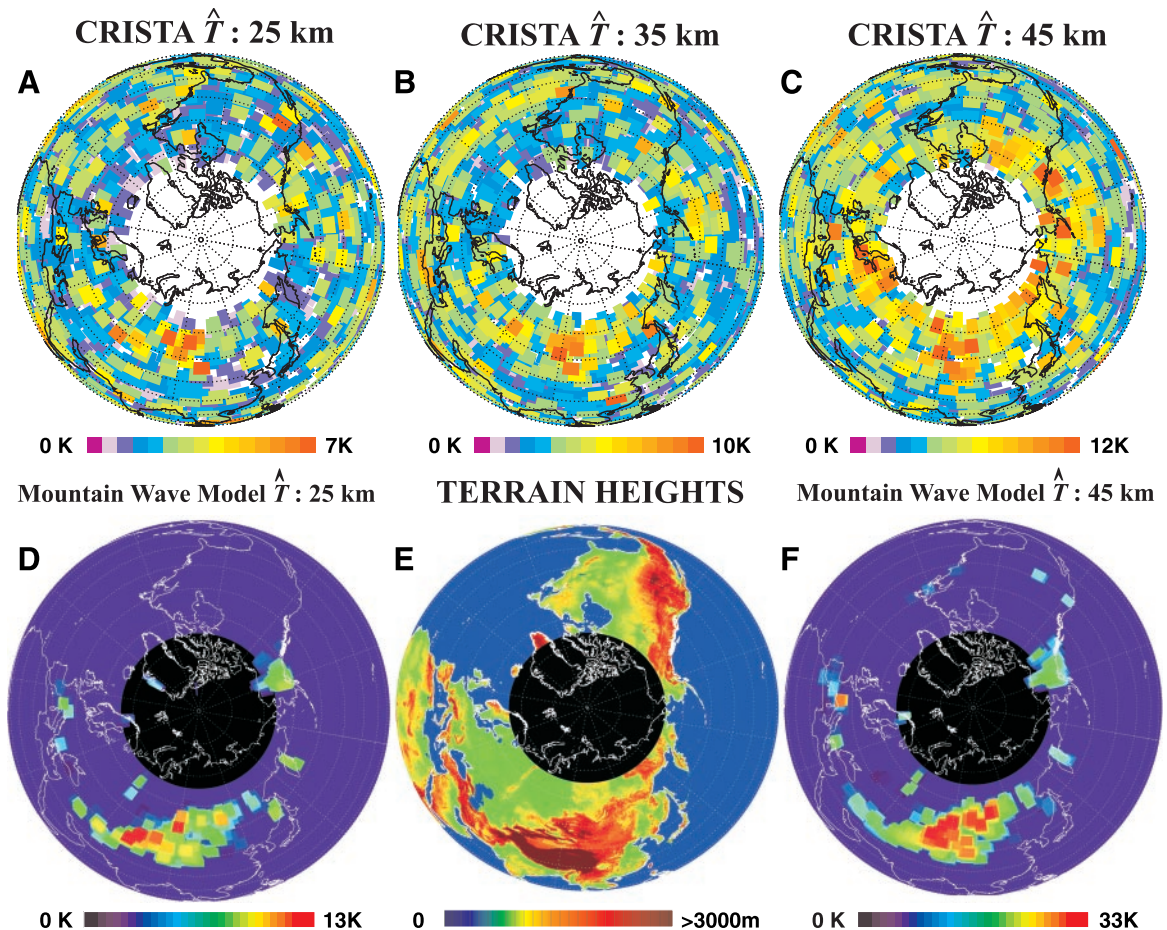
Sayan Ranges, and Tian Shan, which skirt the border regions of Russia, Mongolia, China, and Kazakhstan (Fig. 4E). These mountain waves are present at all heights, reaching the uppermost levels of the stratosphere (Fig. 4C). There is also evidence of more isolated mountain wave activity over the Alps and the Alaska-Yukon region. Mountain waves are largely absent in both the observations and model results over other mountainous regions, such as western North America, the Himalayas, Greenland, and Scandinavia. This absence occurs in the MWFM results because regional winds inhibit mountain wave propagation into the stratosphere.

Despite the basic similarities, specific differences between the CRISTA data and MWFM results are also evident in Figs. 3 and 4. Shortcomings in the model may be implicated here, highlighting the potential value of observations such as these in improving global mountain wave parameterizations.

Figure 4C also shows large $\hat{T}$ amplitudes at $z = 45$ km at the northernmost latitudes, which cannot be explained in terms of polar mountain waves (Fig. 4F). This observation is consistent with large gravity-wave amplitudes observed previously in ground-based soundings of the high-latitude winter upper stratosphere (28). The feature has been attributed to enhanced $\exp(z/2H_\rho)$ amplitude growth of weaker "background" gravity-wave activity, due to the temperature structure of the winter polar stratosphere (13, 29), although longitudinal asymmetries in stratospheric winds can modulate the effect substantially (30). This indicates that CRISTA measured gravity waves from sources other than mountains as well.

References and Notes

1. R. B. Smith, *Adv. Geophys.* **21**, 87 (1979); M. G. Wurtele, R. D. Sharman, A. Datta, *Annu. Rev. Fluid Mech.* **28**, 429 (1996).
2. T. N. Palmer, G. J. Shutts, R. Swinbank, *Q. J. R. Meteorol. Soc.* **112**, 1001 (1986); N. McFarlane, *J. Atmos. Sci.* **44**, 175 (1987); J. Zhou, Y. C. Sud, K.-M. Lau, *Q. J. R. Meteorol. Soc.* **122**, 903 (1996).
3. D. K. Lilly and P. F. Lester, *J. Atmos. Sci.* **31**, 800 (1974).
4. J. T. Bacmeister, P. A. Newman, B. L. Gary, K. R. Chan, *Weather Forecasting* **9**, 241 (1994).
5. F. M. Ralph, P. J. Nieman, D. Levinson, *Geophys. Res. Lett.* **24**, 663 (1997); R. M. Worthington, *J. Atmos. Sol.-Terr. Phys.* **60**, 1543 (1998).
6. J.-F. Lamarque, A. O. Langford, M. H. Proffitt, *J. Geophys. Res.* **101**, 22969 (1996); T. Schilling, F.-J. Lübken, F. G. Wienhold, P. Hoor, H. Fischer, *Geophys. Res. Lett.* **26**, 303 (1999).
7. D. Cariolle, S. Muller, F. Cayla, M. P. McCormick, *J. Geophys. Res.* **94**, 11233 (1989); T. Deshler, T. Peter, R. Müller, P. Crutzen, *Geophys. Res. Lett.* **21**, 1327 (1994); K. S. Carslaw *et al.*, *J. Geophys. Res.* **103**, 5785 (1998); K. S. Carslaw, T. Peter, J. T. Bacmeister, S. D. Eckermann, *J. Geophys. Res.* **104**, 1827 (1999); J. Schreiner *et al.*, *Science* **283**, 968 (1999).
8. K. S. Carslaw *et al.*, *Nature* **391**, 675 (1998).
9. K. Sato, *J. Atmos. Sci.* **47**, 2803 (1990); F. M. Ralph, M. Crochet, S. V. Venkateswaran, *Q. J. R. Meteorol. Soc.* **118**, 597 (1992); R. M. Worthington and L. Thomas, *Geophys. Res. Lett.* **24**, 1071 (1997); C. M. Scavuzzo, M. A. Lamfri, H. Teitelbaum, F. Lott, *J. Geophys. Res.* **103**, 1747 (1998); J. A. Whiteway, *J. Atmos. Sci.* **56**, 1344 (1999).
10. G. J. Shutts and A. Broad, *Q. J. R. Meteorol. Soc.* **119**, 377 (1993); J. L. Attié, A. Druilhet, P. Durand, B. Bénech, *Ann Geophys.* **15**, 823 (1997); J. Dean-Day *et al.*, *Geophys. Res. Lett.* **25**, 1351 (1998).
11. J. T. Bacmeister, M. R. Schoeberl, L. R. Lait, P. A. Newman, B. Gary, *Geophys. Res. Lett.* **17**, 81 (1990); G. D. Nastrom and D. C. Fritts, *J. Atmos. Sci.* **49**, 101 (1992).
12. E. J. Fetzer and J. C. Gille, *J. Atmos. Sci.* **51**, 2461 (1994); D. L. Wu and J. W. Waters, *Geophys. Res. Lett.* **23**, 3631 (1996); R. H. Picard *et al.*, *Geophys. Res. Lett.* **25**, 2809 (1998).
13. M. J. Alexander, *J. Geophys. Res.* **103**, 8627 (1998).
14. D. Offermann *et al.*, *J. Geophys. Res.* **104**, 16311 (1999). CRISTA-SPAS orbited ~100 km behind the shuttle, with the CRISTA telescopes pointed opposite to the orbital motion (backward viewing). The left and right telescopes scanned the limb 18° on either side of the center telescope. This corresponds to tangent heights separated by ~600 km.
15. M. Riese *et al.*, *J. Geophys. Res.* **104**, 16349 (1999).
16. Riese *et al.* (15) give full details of version 1 CRISTA retrievals, which yielded temperatures of ~1 K precision. Data analyzed here come from improved version 2 retrievals (precision of ~0.5 K).
17. P. Preusse, B. Schaeler, J. T. Bacmeister, D. Offermann, *Adv. Space Res.*, in press. Visibility is defined here as the measured wave temperature amplitude divided by its actual amplitude.
18. There were two main measurement modes: a stratosphere mode (77 hours of data every 200 km along track) and a stratosphere-mesosphere mode (55 hours of data every 400 km along track). Additionally, every fourth profile was a high-altitude scan (HAS) (15). HAS data were not analyzed here.
19. See, for example, section 2.1 of D. C. Fritts, *Rev. Geophys.* **22**, 275 (1984).
20. EP flux F is conserved for a nonbreaking, steady plane mountain wave [A. Eliassen and E. Palm, *Geofys. Publ.* **22**, 1 (1961)]. With the use of irrotational hydrostatic gravity-wave relations, it can be evaluated from measured mountain wave variables as

$$ F = \frac{-\rho g \lambda_z \hat{T}^2}{2\overline{T}\lambda_h [d\overline{T}/dz + \Gamma_a]} $$

where ρ is atmospheric density and g is gravitational acceleration. This equation yields a predominantly westward EP flux ~0.02 to 0.2 Pa below 30 km (given the quoted uncertainties in λ_h and $\hat{T}$). When mountain waves break, the vertical EP flux gradient quantifies the force exerted on the atmosphere and the intensity of turbulence generated locally (2, 4, 19, 22).
21. M. J. Alexander and K. Rosenlof, *J. Geophys. Res.* **101**, 23465 (1996).
22. An improved research version of MWFM was used here, which uses ray-tracing methods to better simulate the amplitudes and three-dimensional nonhydrostatic propagation of waves through the atmosphere [S. D. Eckermann and C. J. Marks, *Adv. Space Res.* **20** (no. 6), 1253 (1997)].
23. L. Coy and R. Swinbank, *J. Geophys. Res.* **102**, 25763 (1997).
24. M. Leutbecher and H. Volkert, *Geophys. Res. Lett.* **23**, 3329 (1996); A. Dörnbrack, M. Leutbecher, H. Volkert, M. Wirth, *Meteorol. Appl.* **5**, 117 (1998).
25. CRISTA ozone and trace gas data show this clearly; see Plate 2a of M. Riese *et al.* [*J. Geophys. Res.* **104**, 16349 (1999)] and Plate 5 of M. Riese, X. Tie, G. Brasseur, and D. Offermann [*J. Geophys. Res.* **104**, 16419 (1999)].
26. R. R. Garcia and B. A. Boville, *J. Atmos. Sci.* **51**, 2238 (1994); T. J. Duck, J. A. Whiteway, A. I. Carswell, *Geophys. Res. Lett.* **25**, 2813 (1998).
27. There are a number of reasons for these differences. Although efforts were made to correct for observational smearing of the CRISTA $\hat{T}$ values, measured amplitudes may still be substantially underestimated. Additionally, linear plane-wave parameterizations such as MWFM tend to overestimate wave amplitudes [S. A. Smith, D. C. Fritts, T. E. VanZandt, *J. Atmos. Sci.* **44**, 1404 (1987); G. J. Shutts, *Q. J. R. Meteorol. Soc.* **124**, 1421 (1998)].
28. I. Hirota, *J. Atmos. Terr. Phys.* **46**, 767 (1984); S. D. Eckermann, I. Hirota, W. K. Hocking, *Q. J. R. Meteorol. Soc.* **121**, 149 (1995).
29. S. D. Eckermann, *J. Atmos. Terr. Phys.* **57**, 105 (1995).
30. J. A. Whiteway *et al.*, *Geophys. Res. Lett.* **24**, 1387 (1997).
31. This research was supported by the Office of Naval Research and by NASA through the Atmospheric Chemistry Modeling and Analysis Program and the Upper Atmosphere Research Satellite Guest Investigator Program.

17 June 1999; accepted 19 October 1999

Enhancement of Interdecadal Climate Variability in the Sahel by Vegetation Interaction

Ning Zeng,[1]* J. David Neelin,[1] K.-M. Lau,[2] Compton J. Tucker[2]

The role of naturally varying vegetation in influencing the climate variability in the West African Sahel is explored in a coupled atmosphere–land-vegetation model. The Sahel rainfall variability is influenced by sea-surface temperature variations in the oceans. Land-surface feedback is found to increase this variability both on interannual and interdecadal time scales. Interactive vegetation enhances the interdecadal variation substantially but can reduce year-to-year variability because of a phase lag introduced by the relatively slow vegetation adjustment time. Variations in vegetation accompany the changes in rainfall, in particular the multidecadal drying trend from the 1950s to the 1980s.

The rainfall over the West African Sahel region (1) shows a multidecadal drying trend from the 1950s to the 1980s and early 1990s, as well as strong interannual variability (Fig. 1A). Causes proposed to explain this dramatic trend include global sea surface temperature (SST) variations (2–5) and land use change, that is, the desertification process (6, 7). Because vegetation distribution tends to be controlled largely by climate (8, 9), and surface property changes can affect climate by modifying the atmospheric energy and water budget (10–13), it is reasonable to propose that dynamic vegetation-climate interaction might influence decadal climate variability substantially in a climatically sensitive zone such as the Sahel. We tested this